

# Geophysical Research Letters



## RESEARCH LETTER

10.1029/2019GL082850

### Key Points:

- Variability in subpolar Southern Ocean sea level is documented using satellite radar altimetry, including in ice-covered areas
- Subpolar Southern Ocean sea level exhibits a phased, bimodal response to circumpolar wind changes, entailing a strong seasonal cycle
- The relevant wind forcing is partially described by the Southern Annular Mode and is modulated by sea ice cover near Antarctica

### Supporting Information:

- Supporting Information S1

### Correspondence to:

A. C. Naveira Garabato,  
acng@noc.soton.ac.uk

### Citation:

Naveira Garabato, A. C., Dotto, T. S., Hooley, J., Bacon, S., Tsamados, M., Ridout, A., et al. (2019). Phased response of the subpolar Southern Ocean to changes in circumpolar winds. *Geophysical Research Letters*, *46*, 6024–6033. <https://doi.org/10.1029/2019GL082850>

Received 15 MAR 2019

Accepted 16 MAY 2019








Accepted article online 23 MAY 2019

Published online 13 JUN 2019

©2019. The Authors.

This is an open access article under the terms of the Creative Commons Attribution License, which permits use, distribution and reproduction in any medium, provided the original work is properly cited.

## Phased Response of the Subpolar Southern Ocean to Changes in Circumpolar Winds

A. C. Naveira Garabato<sup>1</sup> , T. S. Dotto<sup>1</sup>, J. Hooley<sup>1</sup>, S. Bacon<sup>2</sup> , M. Tsamados<sup>3</sup> , A. Ridout<sup>3</sup> , E. E. Frajka-Williams<sup>2</sup> , L. Herraiz-Borreguero<sup>4</sup>, P. R. Holland<sup>5</sup>, H. D. B. S. Heerton<sup>3</sup> , and M. P. Meredith<sup>5</sup> 

<sup>1</sup>Ocean and Earth Science, University of Southampton, Southampton, UK, <sup>2</sup>National Oceanography Centre, Southampton, UK, <sup>3</sup>Centre for Polar Observation and Modelling, University College London, London, UK, <sup>4</sup>CSIRO Oceans and Atmosphere, Hobart, Tasmania, Australia, <sup>5</sup>British Antarctic Survey, Cambridge, UK

**Abstract** The response of the subpolar Southern Ocean (sSO) to wind forcing is assessed using satellite radar altimetry. sSO sea level exhibits a phased, zonally coherent, bimodal adjustment to circumpolar wind changes, involving comparable seasonal and interannual variations. The adjustment is effected via a quasi-instantaneous exchange of mass between the Antarctic continental shelf and the sSO to the north, and a 2-month-delayed transfer of mass between the wider Southern Ocean and the subtropics. Both adjustment modes are consistent with an Ekman-mediated response to variations in surface stress. Only the fast mode projects significantly onto the surface geostrophic flow of the sSO; thus, the regional circulation varies in phase with the leading edge of sSO sea level variability. The surface forcing of changes in the sSO system is partly associated with variations of surface winds linked to the Southern Annular Mode and is modulated by sea ice cover near Antarctica.

### 1. Introduction

The subpolar Southern Ocean (sSO), extending from Antarctica to the southern boundary of the Antarctic Circumpolar Current (Figure 1), is a region of vigorous and complex interactions between the atmosphere, cryosphere, and ocean, with an influence on Earth's climate that is disproportionate to its area. Such interactions are pivotal to the stability of the Antarctic Ice Sheet and global sea level (Jenkins et al., 2018), the volume and area of Antarctic sea ice (Holland & Kwok, 2012), Earth's albedo (Meehl & Washington, 1990), and the production of the Antarctic Bottom Water that cools and ventilates the global ocean abyss (Naveira Garabato et al., 2016). Evidence is mounting that the sSO is undergoing a significant transition in its climatic state and global influence, entailing an intensification of the atmospheric polar vortex (Thompson et al., 2011), accelerated melting of the Antarctic Ice Sheet (Rye et al., 2014; Shepherd et al., 2018), a redistribution of sea ice (Holland, 2014), and extensive warming, freshening, and poleward contraction of Antarctic Bottom Water (Purkey & Johnson, 2012). However, understanding these changes and their mechanistic connections is confounded by the historical scarcity of oceanic measurements in the region, which presents a challenging environment to in situ observing platforms and, through its pervasive sea ice cover, satellite measurements.

Two specific oceanic features of the sSO are fundamental in establishing the region's coupled behavior and climatic role and are thereby priority targets for advances in observation and dynamical understanding. First, a quasi-circumpolar frontal jet (the Antarctic Slope Front; Figure 1) flows westward at the surface along much of the Antarctic continental slope, mediating physical transfers among zonally distant areas of the sSO (Thompson et al., 2019). This frontal system regulates exchanges between the Antarctic continental shelves and the open ocean that are critical to the on-shelf supply of heat governing Antarctic ice shelf melting and sea ice formation and to the production and offshore export of Antarctic Bottom Water at the shelf break. Second, a mid-depth pycnocline extends across large areas of the Antarctic continental shelves (with the exception of confined sites of dense shelf-water formation), separating relatively cold, fresh, and light upper-ocean waters from warmer, saltier, and denser waters originating in the Antarctic Circumpolar Current (Jenkins et al., 2016). Variations in the depth and intensity of the on-shelf pycnocline modulate the access of warm deep waters to the Antarctic ice shelf cavities and pre-condition the local formation of sea ice and the dense shelf-water precursors of Antarctic Bottom Water.

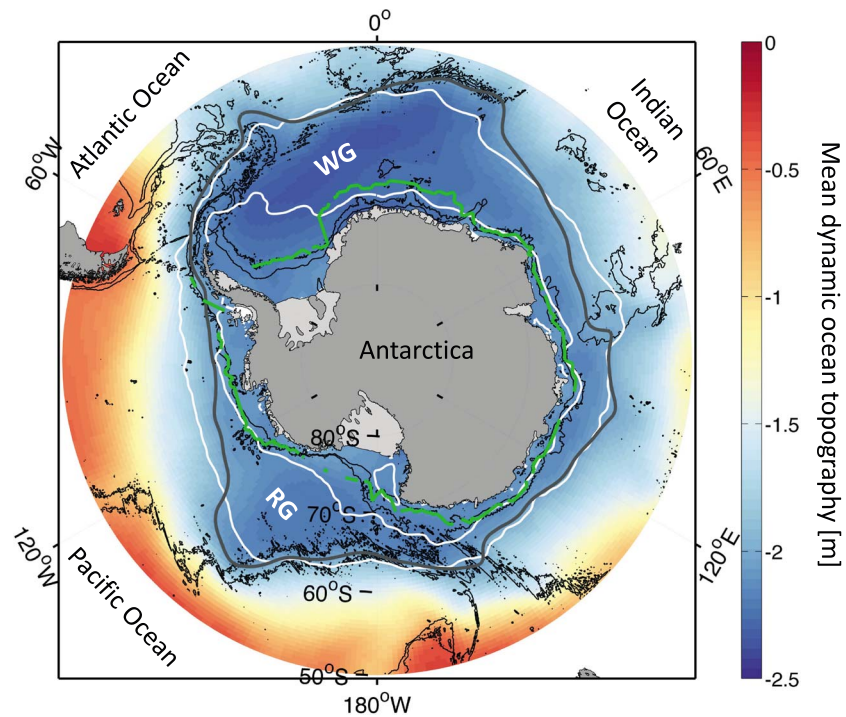


**Figure 1.** Mean dynamic topography of the Southern Ocean (shading) from the EIGEN-6C4 geoid estimate (Förste et al., 2014). The southernmost circumpolar contour ( $-2$  m), bounding the subpolar Southern Ocean to the north, is marked in grey. The minimum cross-slope gradient in dynamic topography close to Antarctica, indicative of the Antarctic Slope Front, is shown (where present) in green. The climatological minimum (January–March) and maximum (July–September) sea ice extents are indicated in white. Selected isobaths (1,000 and 3,000 m) are shown in black. The Weddell and Ross gyres are, respectively, labeled as WG and RG.

As a result of the sSO's environmental challenges to conventional observational approaches, our understanding of the regional ocean dynamics remains fragmentary and is founded primarily on a few long-term mooring records (Daae et al., 2018; Graham et al., 2013; Kim et al., 2016; Núñez-Riboni & Fahrbach, 2009; Peña-Molino et al., 2016; Webber et al., 2017) and numerical models (Kimura et al., 2017; Mathiot et al., 2011; Palocz et al., 2018; Stewart & Thompson, 2015) as well as sparse hydrographic data (Hatterman, 2018; Mallett et al., 2018). These studies indicate that in many areas around Antarctica, the slope frontal system and on-shelf pycnocline exhibit pronounced seasonality, with wind forcing being consistently suggested as the primary causal factor. This basic conceptual understanding was recently corroborated by Armitage et al. (2018) and Dotto et al. (2018), who drew on novel developments in the processing of satellite radar altimetry in ice-covered regions to document the seasonal cycle of sea level and surface geostrophic circulation across the sSO and in the region's Pacific sector, respectively. Those investigations showed that the seasonality unveiled locally by in situ measurements occurs extensively around the sSO and that the observed variability is broadly coherent with wind forcing patterns.

Here we build on these recent studies by assessing the nature and drivers of sSO variability using the new altimetric observations. Our work extends that of Armitage et al. (2018) in that (i) it dissects the adjustment of the sSO to forcing in a way that illuminates the key drivers and dynamics, as well as their divergent impacts on the two major oceanic features of the sSO outlined above, and (ii) it considers the role of sea ice in modulating sSO variability and demonstrates its significance. We show that the sSO responds to circumpolar wind and ice forcing via a phased, zonally coherent, bimodal adjustment involving a quasi-instantaneous exchange of mass between the Antarctic continental shelf and the sSO to the north, and a delayed (2-month-lagged) mass transfer between the wider Southern Ocean and the subtropics. Whereas only the fast mode regulates the intensity of the Antarctic slope frontal jet, both modes influence Antarctic coastal sea level, which is directly coupled to the on-shelf pycnocline via Ekman dynamics (Jenkins et al., 2016; Stewart & Thompson, 2015).

## 2. Data and Methods

### 2.1. Altimetric Data

Gridded along-track sea surface height (SSH) anomaly ( $\eta$ ) data obtained by Cryosat-2 radar altimetry (Wingham et al., 2006) between November 2010 and February 2016 are analyzed. Cryosat-2 operated in three modes: low-resolution mode in the sea ice-free open ocean, synthetic aperture radar over sea ice, and synthetic aperture radar Interferometric near coastal margins. SSH measurements in ice-covered regions were processed following the methodology of Peacock and Laxon (2004), which discriminates between diffuse echoes from sea ice and specular echoes from leads. A seasonal offset between the open-ocean and lead measurements was determined, induced by the different retracers utilized to fit the altimeter return echoes; this was added to the lead data to rectify the bias (Armitage et al., 2016, 2018; Bulczak et al., 2015; Dotto et al., 2018).

The bias-corrected data were mapped onto a spatiotemporal grid with spacings of  $0.5^\circ$  (latitude),  $1^\circ$  (longitude), and 1 month. Zonal ( $u$ ) and meridional ( $v$ ) surface geostrophic velocity anomalies were calculated as

$$u = -gf^{-1}\partial\eta/\partial y \quad (1)$$

and

$$v = gf^{-1}\partial\eta/\partial x, \quad (2)$$

where  $g$  is gravity,  $f$  is the Coriolis parameter, and  $x$  and  $y$  are the meridional distances. The uncertainty for the gridded SSH is 1.5 cm (Dotto et al., 2018).

### 2.2. Assessment of Drivers of Subpolar Southern Ocean Variability

Monthly mean wind stress, wind stress curl, ocean surface stress, and ocean surface stress curl (OSC) were calculated to investigate the drivers of sSO sea level variability. Wind data were acquired from the European Centre for Medium-Range Weather Forecasts ERA-Interim reanalysis (Dee et al., 2011), sea ice concentration data from the National Snow and Ice Data Center (Cavalieri et al., 1996), and sea ice drift data from the Polar Pathfinder Daily Sea Ice Motion (Tschudi et al., 2016). All data sets were interpolated onto the SSH grid and restricted to the period of January 2011 to December 2015, the years for which SSH data are available in all months. Ocean surface stress was computed as follows:

$$\tau = \alpha\tau_{\text{ice-water}} + (1-\alpha)\tau_{\text{air-water}}$$

where

$$\begin{aligned} \tau_{\text{ice-water}} &= \rho_w C_{iw} |\mathbf{u}_i| \mathbf{u}_i \\ \tau_{\text{air-water}} &= \rho_a C_{aw} |\mathbf{u}_a| \mathbf{u}_a \end{aligned}$$

and  $\alpha$  is sea ice concentration,  $\rho_a = 1.25 \text{ kg/m}^3$  air density, and  $\rho_w = 1,028 \text{ kg/m}^3$  seawater density.  $\mathbf{u}_a$  and  $\mathbf{u}_i$ , respectively, indicate the velocities of wind and sea ice drift, and  $C_{iw}$  and  $C_{aw}$  denote ice-water and air-water drag coefficients set to  $5.50 \times 10^{-3}$  and  $1.25 \times 10^{-3}$  (Tsamados et al., 2014). A constant  $C_{iw}$  and a stagnant ocean were assumed. Our results are qualitatively independent of the chosen  $C_{iw}$ .

GRACE RL05-Mascon ocean bottom pressure (OBP) anomalies from the Center for Space Research at the University of Texas (Save et al., 2016) were used to gain insight into the mechanisms of sSO sea level variability. A climatic index characterizing the state of the Southern Annular Mode (SAM) was considered to synthesize the influence of circumpolar winds on the sSO (Thompson & Wallace, 2000). The SAM is the principal mode of atmospheric variability in the extratropical Southern Hemisphere, and entails synchronous, opposing atmospheric pressure anomalies over Antarctica and the midlatitudes.

The relationships between SSH, OBP, and OSC were assessed via maximum covariance analysis (MCA) of each pair of variables using singular value decomposition, whereby the covariance patterns of the cross-covariance matrix are extracted (Wallace et al., 1992). As applied here, MCA determines the spatial patterns in each pair of variables that vary concurrently in time. We performed this analysis for the Southern Ocean south of  $50^\circ\text{S}$ , after subtracting the local mean and linear trend from each data set.

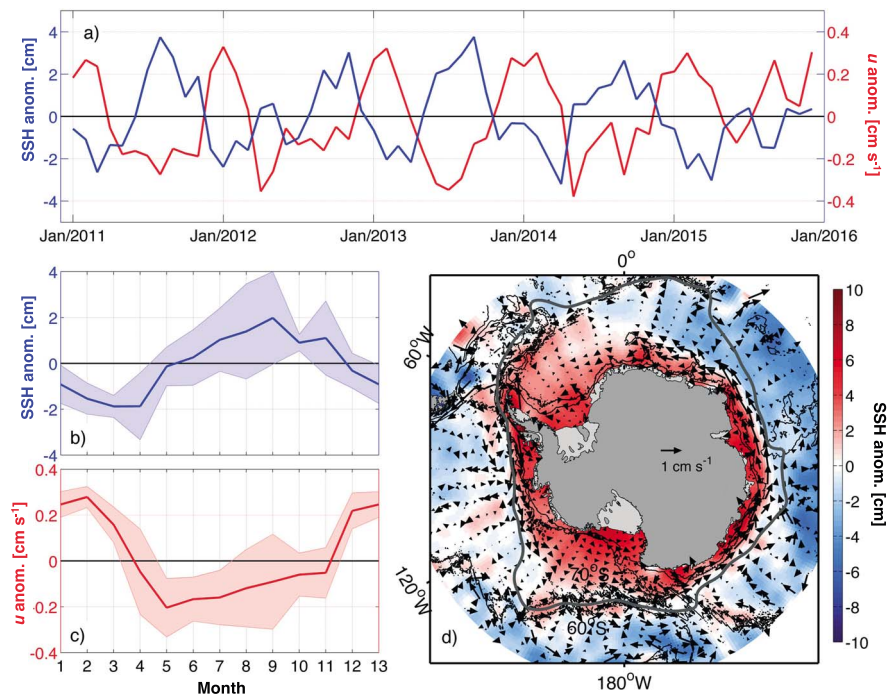


**Figure 2.** (a) Time series of sea surface height (SSH) anomaly (blue) and zonal surface geostrophic velocity anomaly (red) in the subpolar Southern Ocean (sSO) to the south of 60°S. Mean seasonal cycle of (b) SSH anomaly and (c) zonal surface geostrophic velocity anomaly in the same region (lines). Shading indicates one standard deviation of the interannual variability in each month. (d) SSH anomaly (shading) and surface geostrophic velocity anomaly (vectors) in July–September relative to February–April. The northern boundary of the sSO is marked in grey.

### 3. Results

#### 3.1. Subpolar Southern Ocean Variability

sSO SSH displays substantial month-to-month variability (Figures 2a and 2b), which primarily entails a meridional exchange of water between the Antarctic margins and the sSO to the north (Figure 2d). This variability has a standard deviation of ~2 cm near Antarctica and contains a seasonal cycle of range ~5 cm. Highest (lowest) SSH occurs in July–September and lowest (highest) SSH occurs in February–April at the Antarctic coast (in the sSO to the north). The seasonal cycle in sSO SSH varies significantly from one year to another, with the range of interannual variability (~4 cm) being comparable to that of the mean seasonal cycle. These year-to-year variations stem principally from interannual fluctuations in the phase (rather than the amplitude) of the seasonal cycle (Figure 2a).

The variability of the surface geostrophic flow in the sSO is oriented mainly in the zonal direction, as corresponds to a horizontal gradient of SSH anomaly that is aligned approximately perpendicular to the Antarctic coast (Figure 2d). Zonal surface geostrophic flow anomalies are largest at the Antarctic continental slope, where they exhibit a standard deviation of ~0.5 cm/s. Zonal flow anomalies in this region anticovary with more modest anomalies in the sSO to the north (north of ~60°S; Figure 2d), characterized by a standard deviation of ~0.1 cm/s. The variability of the zonal flow is predominantly seasonal (Figures 2a and 2c). Westward (eastward) flow anomalies at the Antarctic continental slope peak at ~1 cm/s in May–July (December–February), in association with maximum eastward (westward) flow anomalies of ~0.3 cm/s in the sSO to the north. Substantial interannual changes in zonal flow also occur, with the range of interannual variability (~0.5 cm/s) being almost as large as that of the mean seasonal cycle. As for SSH, interannual variations in zonal flow mainly originate from year-to-year changes in the phase of the seasonal cycle (Figure 2a).

The seasonal variations in sSO SSH and surface geostrophic flow are broadly synchronous. However, their seasonal cycles exhibit a phase shift, whereby the strongest (weakest) westward flow at the Antarctic continental slope leads the highest (lowest) on-shelf SSH by 1–3 months (Figures 2b and 2c). This phase difference

appears at odds with the dynamical relation between the two variables (equations (1) and (2)), from which the largest SSH anomalies on the shelf (Figure 2d) might be expected to occur concurrently to the largest flow anomalies on the continental slope. We will show that the observed phase shift stems from the adjustment of sSO SSH to changes in atmospheric and cryospheric forcing via two distinct dynamical responses, of which only one has a notable impact on surface geostrophic flow.

### 3.2. Relationship of Subpolar Southern Ocean Variability to Surface Forcing

Wind forcing has been extensively shown to exert a dominant control on SSH variability across the Southern Ocean on the intra-annual to interannual timescales considered here (Hughes et al., 1999, 2003; Kushahara & Ohshima, 2009; Zika et al., 2013). However, in the sSO, where sea ice is seasonally pervasive, the momentum transfer from the wind to the ocean is likely to be significantly modulated by ice cover (Martin et al., 2014; Tsamados et al., 2014). The joint role of wind and sea ice in regulating sSO variability is thus assessed by conducting a MCA of OSC and each of the pertinent oceanic variables. Although steric effects are not explicitly considered here, their relative insignificance can be surmised from our observation (Figure 2b) of maximum (minimum) SSH along the Antarctic margins in late winter (summer), when upper-ocean waters are densest (lightest) (Mallett et al., 2018; Núñez-Riboni & Fahrback, 2009) and the steric contribution to SSH is minimum (maximum).

The MCA of SSH and OSC reveals that 64% of the squared covariance between these variables is explained by two modes (Figures 3a–3d). These modes are comparable in amplitude, entailing SSH changes of range 3–4 cm, and exhibit a broadly annular footprint. The meridional structure of the modes is, however, distinct. The first mode ( $MCA1_{SSH,OSC}$ ) involves an anticovariation in SSH between the bulk of the sSO and the Southern Ocean to the north, with maximum SSH ranges inshore of the Antarctic continental slope (Figure 3a). This mode is also captured by the first empirical orthogonal function mode of SSH (Figure S1a), which accounts for 24% of the total SSH variance. The second mode ( $MCA2_{SSH,OSC}$ ) consists of an anticovariation in SSH between the bulk of the Southern Ocean and some of the basins to the north (specifically, the areas around South America, Africa, and Australasia, north of  $\sim 55^\circ S$ ) as well as, in less pronounced form, the inner reaches of the Antarctic continental shelf (Figure 3c). This mode also emerges as the second empirical orthogonal function mode of SSH (Figure S1b), which accounts for 12% of the total SSH variance. The two modes have broadly similar seasonal cycles (Figures 3e and 3f) yet display a significant difference in phase, whereby  $MCA2_{SSH,OSC}$  lags  $MCA1_{SSH,OSC}$  by several months. The superposition of these de-phased modes gives rise to the seasonal cycle in sSO SSH.

## 4. Discussion

While the modes produced by the MCA of SSH and OSC are statistical constructs, several lines of evidence suggest that they describe distinct dynamical responses of the Southern Ocean to circumpolar wind and sea ice forcing.  $MCA1_{SSH,OSC}$  is consistent with a wind- and ice-driven exchange of mass between the Antarctic continental shelf and the Southern Ocean to the north. Variations in sSO SSH associated with this mode correspond closely in space with anomalies in OSC of the same sign (Figures 3a and 3b), as expected from a quasi-instantaneous oceanic response to changes in surface stress mediated by Ekman dynamics. The circumpolar coherence of SSH variations around the Antarctic continental shelf is indicative of the fast propagation of sea level fluctuations along the almost-closed barotropic potential vorticity contours that encircle Antarctica, via topographic waves (Hughes et al., 1999; Kushahara & Ohshima, 2009; Spence et al., 2017). The mode of SSH variability characterized by  $MCA1_{SSH,OSC}$  has been documented with bottom pressure recorder and tide gauge data as well as numerical models and is often termed the “southern mode” (Aoki, 2002; Hughes et al., 1999, 2003).

$MCA2_{SSH,OSC}$  is consistent with a wind- and ice-driven exchange of mass between the Southern Ocean and, primarily, the basins to the north. As for the first mode, variations in SSH described by  $MCA2_{SSH,OSC}$  (Figure 3c) are associated with a broadly annular pattern of surface stress (Figure 3d). This surface stress curl distribution resembles that of  $MCA1_{SSH,OSC}$ , with some substantial differences in the South Atlantic, Southwest Indian, and central South Pacific sectors. The spatial correlation between the SSH and OSC anomaly fields is reduced for  $MCA2_{SSH,OSC}$  ( $r = 0.42$ ) relative to  $MCA1_{SSH,OSC}$  ( $r = 0.52$ ) and thereby suggests that  $MCA2_{SSH,OSC}$  does not simply describe an instantaneous Ekman-mediated response of SSH to

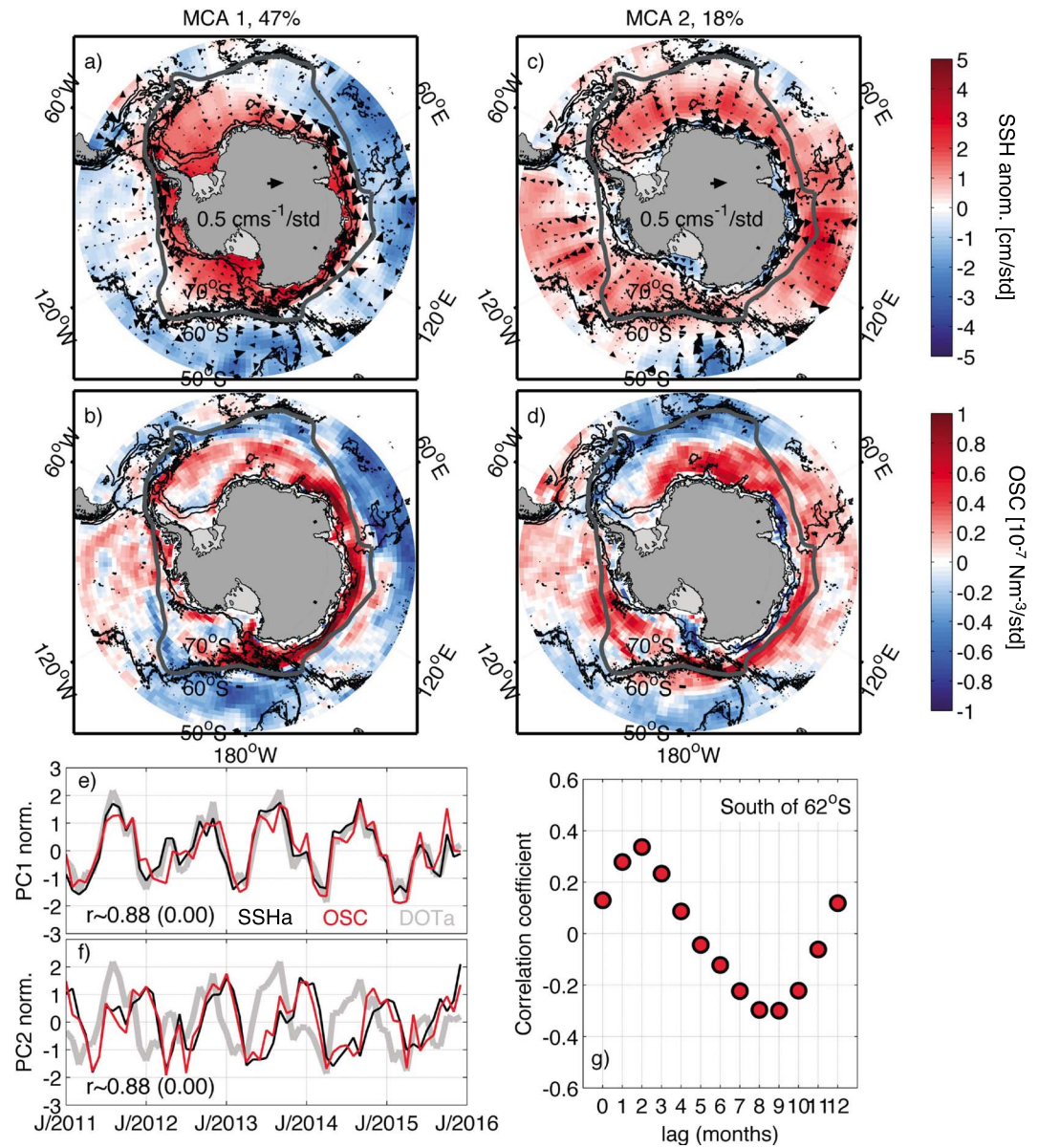


**Figure 3.** Spatial patterns of (a) sea surface height (SSH) anomaly and (b) ocean surface stress curl (OSC) anomaly associated with  $\text{MCA1}_{\text{SSH,OSC}}$  and of (c) SSH anomaly and (d) OSC anomaly associated with  $\text{MCA2}_{\text{SSH,OSC}}$ . The spatial pattern of surface geostrophic velocity anomaly corresponding to that of SSH anomaly is indicated by vectors in (a) and (c). The fraction of the squared covariance between SSH and OSC explained by each mode is indicated in the upper axis of (a) and (c). The northern boundary of the subpolar Southern Ocean (sSO) is marked in grey in each map. Time series of the principal components of SSH anomaly (denoted SSHa, in black) and OSC anomaly (in red) associated with (e)  $\text{MCA1}_{\text{SSH,OSC}}$  and (f)  $\text{MCA2}_{\text{SSH,OSC}}$ . The correlation coefficient ( $r$ ) between SSHa and OSC is indicated in each panel, with the associated  $p$  value in brackets. The original time series of SSH anomaly (denoted DOTa, in grey) shown in Figure 2a is reproduced for reference. (g) Spatial average (over the sSO to the south of  $62^\circ\text{S}$ ) of the coefficient of temporal correlation between the principal component of SSH anomaly associated with  $\text{MCA2}_{\text{SSH,OSC}}$  and the total OSC, at a range of temporal lags (with OSC leading). MCA = maximum covariance analysis.

changes in surface stress. In order to evaluate the possibility that  $\text{MCA2}_{\text{SSH,OSC}}$  may instead represent a lagged response in the sSO system, we quantify the temporal correlation between that mode's principal component of SSH anomaly and the total OSC anomaly at a range of lags (Figure 3g). Initially, correlation rises with increasing lag (with OSC leading SSH) and peaks at 2 months. This suggests that  $\text{MCA2}_{\text{SSH,OSC}}$  describes a 2-month-lagged, Ekman-mediated adjustment of SSH to changes in wind and sea ice forcing.

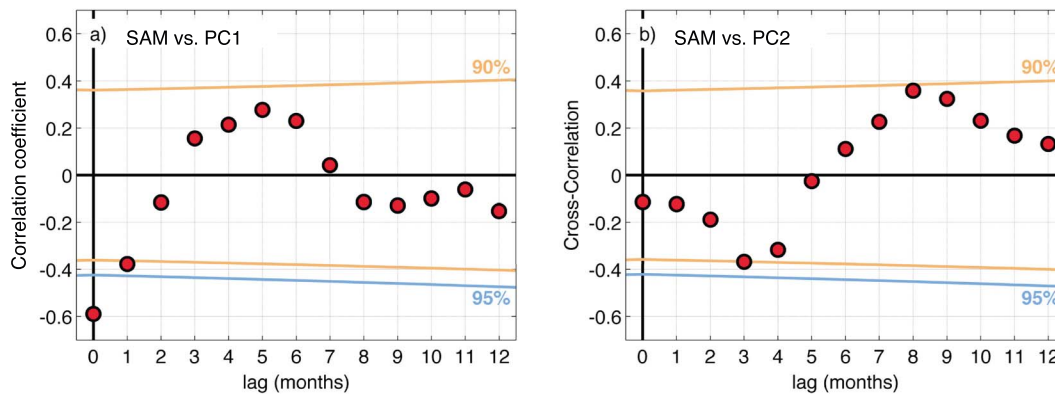


**Figure 4.** Coefficient of correlation (red circles) between the Southern Annular Mode (SAM) index and the principal components (PC) of sea surface height (SSH) anomaly associated with (a)  $MCA1_{SSH,OSC}$  and (b)  $MCA2_{SSH,OSC}$ , as a function of lag (with SAM index leading). The levels of 90% and 95% significance (Sciremammano, 1979) are respectively indicated by orange and blue lines. MCA = maximum covariance analysis, OSC = ocean surface stress curl.

This interpretation is endorsed and augmented by two further results. First, the spatial distribution of the coefficient of temporal correlation between OSC and the  $MCA2_{SSH,OSC}$  principal component for SSH at a lag of 2 months reproduces the structure of the OSC anomaly in  $MCA1_{SSH,OSC}$ , to a greater degree than does the analogous instantaneous correlation (Figures S2, 3b, and 3d). This suggests that  $MCA1_{SSH,OSC}$  and  $MCA2_{SSH,OSC}$  represent de-phased responses (at lags of 0 and 2 months, respectively) of Southern Ocean SSH to the same circumpolar pattern of surface forcing. Second, MCAs of OBP and OSC (Figure S3), and of OBP and SSH (Figure S4), both yield a leading mode that explains a high fraction (57% and 59%, respectively) of the squared covariance between each pair of variables and that is nearly identical to  $MCA2_{SSH,OSC}$  (Figures 3c and 3d). This is consistent with  $MCA2_{SSH,OSC}$  entailing a displacement of a much greater oceanic mass than  $MCA1_{SSH,OSC}$  (as deduced from the much more extensive area of coherent SSH variation within the Southern Ocean apparent in  $MCA2_{SSH,OSC}$ ; Figures 3a and 3c) and thus provides a plausible explanation of the significant lag in the SSH adjustment to surface stress implicit in  $MCA2_{SSH,OSC}$ .

To rationalize the difference in phase between the seasonal cycles of sSO SSH and surface geostrophic flow, we consider the flow anomaly fields associated with  $MCA1_{SSH,OSC}$  and  $MCA2_{SSH,OSC}$  (Figures 3a and 3c). The characteristic magnitude of the flow anomaly linked to  $MCA1_{SSH,OSC}$  considerably exceeds that related to  $MCA2_{SSH,OSC}$ , particularly near the Antarctic continental slope where horizontal gradients of SSH anomaly are largest. This indicates that the mode of SSH variability described by  $MCA1_{SSH,OSC}$  (the “southern mode”) underpins the bulk of the observed changes in surface geostrophic flow and explains the alignment of the seasonal cycle of the flow with that of  $MCA1_{SSH,OSC}$ . This result is supported by the outcome of a MCA of zonal flow and OSC (Figure S5), which reveals that the leading mode ( $MCA1_{u,OSC}$ , accounting for 31% of the squared covariance between the two variables) reproduces the spatial structure of the zonal flow associated with  $MCA1_{SSH,OSC}$  (Figure 3a) and is in phase with  $MCA1_{SSH,OSC}$ .

A notable finding of our analysis is that the representation of the role of sea ice in modulating the transfer of wind momentum to the ocean is essential to adequately capture the response of the sSO (in particular, the oceanic regions closest to Antarctica and the Weddell and Ross gyres; Figure 1) to surface forcing. In those areas, frequent sea ice cover partially suppresses the wind momentum input to the ocean, especially as sea ice drift reduces toward the Antarctic margins. The regional significance of this shielding effect may be illustrated by repeating the above MCA exercises with wind stress curl in lieu of OSC (Figure S6). These show that the close spatial correspondence between patterns of SSH and OSC variability, expected from Ekman dynamics, breaks down across the sSO as OSC is replaced by wind stress curl. Accordingly, the spatial correlation in the sSO to the south of the winter sea ice edge reduces from 0.38 ( $p = 0.05$ ) between SSH and OSC to 0.28 ( $p = 0.15$ ) between SSH and wind stress curl.

To conclude, the surface forcing responsible for driving the sSO variability documented here has an annular structure (Figures 3b and 3d) reminiscent of that of the SAM. The significant association with this mode of large-scale atmospheric variability is confirmed by computing the correlation between the SAM index and each of the  $MCA1_{SSH,OSC}$  and  $MCA2_{SSH,OSC}$  principal components for OSC, at a range of lags (Figure 4).

Whereas for  $MCA1_{SSH,OSC}$  the maximum correlation ( $r = -0.59$ ,  $p = 0.01$ ) occurs at zero lag, for  $MCA2_{SSH,OSC}$  the highest correlation ( $r = -0.38$ ,  $p = 0.10$ ) is found at a lag of 3 months. This endorses our result that  $MCA1_{SSH,OSC}$  and  $MCA2_{SSH,OSC}$ , respectively, represent fast and delayed responses to circumpolar surface forcing and extends our interpretation by suggesting that this forcing is partially described by the SAM. Other forms of variability in circumpolar winds near Antarctica (such as changes in the coastal easterlies linked to katabatic winds; Hazel & Stewart, 2019) are also expected to contribute to the surface forcing of the sSO.

## 5. Conclusions

We have used Cryosat-2 altimetry to show that sSO sea level undergoes a phased, zonally coherent, bimodal adjustment to circumpolar wind and ice forcing, entailing a prominent seasonal cycle and almost equally strong interannual variability. The adjustment is effected via a quasi-instantaneous exchange of mass between the Antarctic continental shelf and the Southern Ocean to the north (the “southern mode”) and a delayed (2-month-lagged) transfer of mass between the wider Southern Ocean and the subtropics. Both adjustment modes are consistent with an Ekman-mediated response to variations in surface stress, with the lag in the delayed mode likely stemming from that mode’s displacement of a very large oceanic mass. As only the fast mode projects strongly onto the sSO surface geostrophic flow, the regional circulation varies in phase with the leading edge of sSO sea level variability. The relevant surface forcing for changes in the sSO system is associated in part with variations of surface winds described by the SAM and is modulated by sea ice cover near Antarctica.

These findings have several important implications for our understanding of the sSO and the representation of the system’s future evolution by climate-scale ocean models. First, the pronounced imprint of circumpolar winds on the physical configuration of the sSO highlights a potential vulnerability of ocean processes near Antarctica (including those controlling global abyssal ocean ventilation, Antarctic sea ice extent, and Antarctic Ice Sheet melting) to contemporary climatic change, which is projected to involve a contraction and strengthening of the polar vortex driven by rising atmospheric greenhouse gas levels (Thompson et al., 2011). Second, the partial dissociation between the responses of sSO sea level and surface circulation to circumpolar winds suggests that future variations in the region’s two key oceanic features (the depth of the on-shelf pycnocline and the intensity of the Antarctic slope frontal jet) may be asynchronous or structurally complex. Third, the significant influence of sea ice in regulating the transfer of wind momentum to the sSO points to the existence of intricate atmosphere-sea ice-ocean feedbacks in the system and stresses the need for their comprehensive characterization. In this context, it is notable that Antarctic sea ice, having undergone a small interdecadal increase in extent, has recently exhibited the three lowest-extent summers on record (Schlosser et al., 2018; Turner et al., 2017). While the level to which these three years might represent the start of a longer trend is presently unclear, these events emphasize that climatic changes in Antarctic sea ice are expected (Bracegirdle et al., 2018) and will impact the momentum transfer to, and dynamical response of, the sSO.

## References

- Aoki, S. (2002). Coherent sea level response to the Antarctic Oscillation. *Geophysical Research Letters*, 29(20), 1950. <https://doi.org/10.1029/2002GL015733>
- Armitage, T. W. K., Bacon, S., Ridout, A. L., Thomas, S. F., Aksenov, Y., & Wingham, D. J. (2016). Arctic sea surface height variability and change from satellite radar altimetry and GRACE, 2003–2014. *Journal of Geophysical Research: Oceans*, 121, 4303–4322. <https://doi.org/10.1002/2015JC011579>
- Armitage, T. W. K., Kwok, R., Thompson, A. F., & Cunningham, G. (2018). Dynamic topography and sea level anomalies of the Southern Ocean: Variability and teleconnections. *Journal of Geophysical Research: Oceans*, 123, 613–630. <https://doi.org/10.1002/2017JC013534>
- Bracegirdle, T. J., Hyder, P., & Holmes, C. R. (2018). CMIP5 diversity in southern westerly jet projections related to historical sea ice area: Strong link to strengthening and weak link to shift. *Journal of Climate*, 31(1), 195–211. <https://doi.org/10.1175/jcli-d-17-0320.1>
- Bulczak, A. I., Bacon, S., Naveira Garabato, A. C., Ridout, A., Sonnewald, M. J. P., & Laxon, S. W. (2015). Seasonal variability of sea surface height in the coastal waters and deep basins of the Nordic Seas. *Geophysical Research Letters*, 42, 113–120. <https://doi.org/10.1002/2014GL061796>
- Cavaliere, D. J., Parkinson, C. L., Gloersen, P., & Zwally, H. J. (1996). Sea ice concentrations from Nimbus-7 SMMR and DMSR SSM/I-SSMIS passive microwave data, version 1. [2010–2016, 50–90°S], Boulder, CO: NASA National Snow and Ice Data Center Distributed Active Archive Center. <https://doi.org/10.5067/8GQ8LZQVLOVL>. Updated yearly (last access: 30 June 2017).
- Daae, K., Darelius, E., Fer, I., Østerhus, S., & Ryan, S. (2018). Wind stress mediated variability of the Filchner Trough overflow, Weddell Sea. *Journal of Geophysical Research: Oceans*, 123, 3186–3203. <https://doi.org/10.1002/2017jc013579>

## Acknowledgments

The CryoSat-2 data were obtained from the European Space Agency (<https://earth.esa.int/web/guest/data-access/>) and processed at CPOM (UCL). The NASA Team ice concentration and sea ice drift data are available from the National Snow and Ice Data Center at <https://nsidc.org/data/nsidc-0051/> and <https://nsidc.org/data/nsidc-0116/>, respectively. ERA-Interim data are available from ECMWF (<https://apps.ecmwf.int/datasets/data/interim-full-daily/levtype=sfc/>). The SAM index is available from NOAA/CPC ([https://www.cpc.ncep.noaa.gov/products/precip/CWlink/daily\\_ao\\_index/aao/aao\\_index.html](https://www.cpc.ncep.noaa.gov/products/precip/CWlink/daily_ao_index/aao/aao_index.html)). GRACE data are available from CSR ([http://www2.csr.utexas.edu/grace/RL05\\_mascons.html](http://www2.csr.utexas.edu/grace/RL05_mascons.html)). J. Hooley acknowledges support by the U.K. Natural Environment Research Council (NERC) SPITFIRE Doctoral Training Partnership and T. S. Dotto by a CNPq/Brazil PhD scholarship (grant 232792/2014-3). The participation of A. C. Naveira Garabato was supported by the Royal Society and the Wolfson Foundation. This work was supported by the NERC ORCHESTRA program (grant NE/N018095/1). Geostrophic flow data presented in this manuscript can be accessed via [http://www.cpom.ucl.ac.uk/dynamic\\_topography](http://www.cpom.ucl.ac.uk/dynamic_topography).



- Dee, D. P., Uppala, S. M., Simmons, A. J., Berrisford, P., Poli, P., Kobayashi, S., et al. (2011). The ERA-Interim reanalysis: Configuration and performance of the data assimilation system. *Quarterly Journal of the Royal Meteorological Society*, *137*(656), 553–597. <https://doi.org/10.1002/qj.828>
- Dotto, T. S., Naveira Garabato, A. C., Bacon, S., Tsamados, M., Holland, P. R., Hooley, J., et al. (2018). Variability of the Ross Gyre, Southern Ocean: Drivers and responses revealed by satellite altimetry. *Geophysical Research Letters*, *45*, 6195–6204. <https://doi.org/10.1029/2018GL078607>
- Förste, C., Bruinsma, S. L., Abrikosov, O., Lemoine, J.-M., Marty, J. C., Flechtner, F., et al. (2014). EIGEN-6C4: The latest combined global gravity field model including GOCE data up to degree and order 2190 of GFZ Potsdam and GRGS Toulouse. *GFZ Data Services*. <https://doi.org/10.5880/icgem.2015.1>
- Graham, J. A., Heywood, K. J., Chavanne, C. P., & Holland, P. R. (2013). Seasonal variability of water masses and transport on the Antarctic continental shelf and slope in the southeastern Weddell Sea. *Journal of Geophysical Research: Oceans*, *118*, 2201–2214. <https://doi.org/10.1002/jgrc.20174>
- Hatterman, T. (2018). Antarctic thermocline dynamics along a narrow shelf with easterly winds. *Journal of Physical Oceanography*, *48*(10), 2419–2443. <https://doi.org/10.1175/jpo-d-18-0064.1>
- Hazel, J. E., & Stewart, A. L. (2019). Are the near-Antarctic easterly winds weakening in response to enhancement of the Southern Annular Mode? *Journal of Climate*, *32*(6), 1895–1918. <https://doi.org/10.1175/jcli-d-18-0402.1>
- Holland, P. R. (2014). The seasonality of Antarctic sea ice trends. *Geophysical Research Letters*, *41*, 4230–4237. <https://doi.org/10.1002/2014GL060172>
- Holland, P. R., & Kwok, R. (2012). Wind-driven trends in Antarctic sea-ice drift. *Nature Geoscience*, *5*(12), 872–875. <https://doi.org/10.1038/ngeo1627>
- Hughes, C. W., Meredith, M. P., & Heywood, K. J. (1999). Wind driven transport fluctuations through Drake Passage: A southern mode. *Journal of Physical Oceanography*, *29*(8), 1971–1992. [https://doi.org/10.1175/1520-0485\(1999\)029<1971:WDTFTD>2.0.CO;2](https://doi.org/10.1175/1520-0485(1999)029<1971:WDTFTD>2.0.CO;2)
- Hughes, C. W., Woodworth, P. L., Meredith, M. P., Stepanov, V., Whitworth, T., & Pyne, A. R. (2003). Coherence of Antarctic sea levels, Southern Hemisphere annular mode, and flow through Drake Passage. *Geophysical Research Letters*, *30*(9), 1464. <https://doi.org/10.1029/2003gl017240>
- Jenkins, A., Dutrieux, P., Jacobs, S., Steig, E. J., Gudmundsson, G. H., Smith, J., & Heywood, K. J. (2016). Decadal ocean forcing and Antarctic ice sheet response: Lessons from the Amundsen Sea. *Oceanography*, *29*(4), 106–117. <https://doi.org/10.5670/oceanog.2016.103>
- Jenkins, A., Shoosmith, D., Dutrieux, P., Jacobs, S., Kim, T. W., Lee, S. H., et al. (2018). West Antarctic Ice Sheet retreat in the Amundsen Sea driven by decadal oceanic variability. *Nature Geoscience*, *11*(10), 733–738. <https://doi.org/10.1038/s41561-018-0207-4>
- Kim, C. S., Kim, T. W., Cho, K. H., Ha, H. K., Lee, S. H., Kim, H. C., & Lee, J. H. (2016). Variability of the Antarctic coastal current in the Amundsen Sea. *Estuarine, Coastal and Shelf Science*, *181*, 123–133. <https://doi.org/10.1016/j.ecss.2016.08.004>
- Kimura, S., Jenkins, A., Regan, H., Holland, P. R., Assman, K. M., Whitt, D. B., et al. (2017). Oceanographic controls on the variability of ice-shelf basal melting and circulation of glacial meltwater in the Amundsen Sea Embayment, Antarctica. *Journal of Geophysical Research: Oceans*, *122*, 10,131–10,155. <https://doi.org/10.1002/2017JC012926>
- Kusahara, K., & Ohshima, K. I. (2009). Dynamics of the wind-driven sea level variation around Antarctica. *Journal of Physical Oceanography*, *39*(3), 658–674. <https://doi.org/10.1175/2008jpo3982.1>
- Mallett, H. K. W., Boehme, L., Fedak, M., Heywood, K. J., Stevens, D. P., & Roquet, F. (2018). Variation in the distribution and properties of Circumpolar Deep Water in the eastern Amundsen Sea, on seasonal timescales, using seal-borne tags. *Geophysical Research Letters*, *45*, 4982–4990. <https://doi.org/10.1029/2018GL077430>
- Martin, T., Steele, M., & Zhang, J. (2014). Seasonality and long-term trend of Arctic Ocean surface stress in a model. *Journal of Geophysical Research: Oceans*, *119*, 1723–1738. <https://doi.org/10.1002/2013JC009425>
- Mathiot, P., Goosse, H., Fichfet, T., Barnier, B., & Gallée, H. (2011). Modelling the seasonal variability of the Antarctic Slope Current. *Ocean Science*, *7*(4), 455–470. <https://doi.org/10.5194/os-7-455-2011>
- Meehl, G. A., & Washington, W. M. (1990). CO<sub>2</sub> climate sensitivity and snow-sea-ice albedo parameterization in an atmospheric GCM coupled to a mixed-layer ocean model. *Climatic Change*, *16*(3), 283–306. <https://doi.org/10.1007/BF00144505>
- Naveira Garabato, A. C., Zika, J. D., Jullion, L., Brown, P. J., Holland, P. R., Meredith, M. P., & Bacon, S. (2016). The thermodynamic balance of the Weddell Gyre. *Geophysical Research Letters*, *43*, 317–325. <https://doi.org/10.1002/2015GL066658>
- Núñez-Riboni, I., & Fahrbach, E. (2009). Seasonal variability of the Antarctic Coastal Current and its driving mechanisms in the Weddell Sea. *Deep Sea Research Part I: Oceanographic Research Papers*, *56*(11), 1927–1941. <https://doi.org/10.1016/j.dsr.2009.06.005>
- Palocz, A., Gille, S. T., & McClean, J. L. (2018). Oceanic heat delivery to the Antarctic continental shelf: Large-scale, low-frequency variability. *Journal of Geophysical Research: Oceans*, *123*, 7678–7701. <https://doi.org/10.1029/2018JC014345>
- Peacock, N. R., & Laxon, S. W. (2004). Sea surface height determination in the Arctic Ocean from ERS altimetry. *Journal of Geophysical Research*, *109*, C07001. <https://doi.org/10.1029/2001JC001026>
- Peña-Molino, B., McCartney, M. S., & Rintoul, S. R. (2016). Direct observations of the Antarctic Slope Current transport at 113°E. *Journal of Geophysical Research: Oceans*, *121*, 7390–7407. <https://doi.org/10.1002/2015JC011594>
- Purkey, S. G., & Johnson, G. C. (2012). Global contraction of Antarctic Bottom Water between the 1980s and 2000s. *Journal of Climate*, *25*(17), 5830–5844. <https://doi.org/10.1175/jcli-d-11-00612.1>
- Rye, C. D., Naveira Garabato, A. C., Holland, P. R., Meredith, M. P., Nurser, A. J. G., Hughes, C. W., et al. (2014). Rapid sea-level rise along the Antarctic margins in response to increased glacial discharge. *Nature Geoscience*, *7*(10), 732–735. <https://doi.org/10.1038/ngeo2230>
- Save, H., Bettadpur, S., & Tapley, B. D. (2016). High-resolution CSR GRACE RL05-Mascon. *Journal of Geophysical Research: Solid Earth*, *121*, 7547–7569. <https://doi.org/10.1002/2016JB013007>
- Schlosser, E., Haumann, F. A., & Raphael, M. N. (2018). Atmospheric influences on the anomalous 2016 Antarctic sea ice decay. *The Cryosphere*, *12*(3), 1103–1119. <https://doi.org/10.5194/tc-12-1103-2018>
- Sciremammano, F. Jr. (1979). A suggestion for the presentation of correlations and their significance levels. *Journal of Physical Oceanography*, *9*(6), 1273–1276. [https://doi.org/10.1175/1520-0485\(1979\)009<1273:ASFTPO>2.0.CO;2](https://doi.org/10.1175/1520-0485(1979)009<1273:ASFTPO>2.0.CO;2)
- Shepherd, A., Ivins, E., Rignot, E., Smith, B., van den Broeke, M., Velicogna, I., et al. (2018). Mass balance of the Antarctic Ice Sheet from 1992 to 2017. *Nature*, *558*(7709), 219–222. <https://doi.org/10.1038/s41586-018-0179-y>
- Spence, P., Holmes, R. M., Hogg, A. M., Griffies, S. M., Stewart, K. D., & England, M. H. (2017). Localized rapid warming of West Antarctic subsurface waters by remote winds. *Nature Climate Change*, *7*(8), 595–603. <https://doi.org/10.1038/nclimate3335>
- Stewart, A. L., & Thompson, A. F. (2015). Eddy-mediated transport of warm Circumpolar Deep Water across the Antarctic shelf break. *Geophysical Research Letters*, *42*, 432–440. <https://doi.org/10.1002/2014GL062281>

- Thompson, A. F., Stewart, A. L., Spence, P., & Heywood, K. J. (2019). The Antarctic Slope Current in a changing climate. *Reviews of Geophysics*, *56*, 741–770. <https://doi.org/10.1029/2018RG000624>
- Thompson, D. W. J., Solomon, S., Kushner, P. J., England, M. H., Grise, K. M., & Karoly, D. J. (2011). Signatures of the Antarctic ozone hole in Southern Hemisphere surface climate change. *Nature Geoscience*, *4*(11), 741–749. <https://doi.org/10.1038/ngeo1296>
- Thompson, D. W. J., & Wallace, J. M. (2000). Annular modes in the extratropical circulation. Part I: Month-to-month variability. *Journal of Climate*, *13*, 1000–1016. [https://doi.org/10.1175/1520-0442\(2000\)013,1000:AMITEC.2.0.CO;2](https://doi.org/10.1175/1520-0442(2000)013,1000:AMITEC.2.0.CO;2)
- Tsamados, M., Feltham, D. L., Schroeder, D., Flocco, D., Farrell, S. L., Kurtz, N., et al. (2014). Impact of variable atmospheric and oceanic form drag on simulations of Arctic sea ice. *Journal of Physical Oceanography*, *44*(5), 1329–1353. <https://doi.org/10.1175/JPO-D-13-0215.1>
- Tschudi, M., Fowler, C., Maslanik, J., Stewart, J. S., & Meier, W. (2016). Polar Pathfinder daily 25 km EASE-grid sea ice motion vectors, version 3. [2010–2016, 50–90°S]. Boulder, CO: NASA National Snow and Ice Data Center Distributed Active Archive Center. <https://doi.org/10.5067/O57VAIT2AYYY> (last access: 27 June 2017).
- Turner, J., Phillips, T., Marshall, G. J., Hosking, J. S., Pope, J. O., Bracegirdle, T. J., & Deb, P. (2017). Unprecedented springtime retreat of Antarctic sea ice in 2016. *Geophysical Research Letters*, *44*, 6868–6875. <https://doi.org/10.1002/2017GL073656>
- Wallace, J. M., Smith, C., & Bretherton, C. S. (1992). Singular value decomposition of wintertime sea surface temperature and 500-mb height anomalies. *Journal of Climate*, *5*(6), 561–576. [https://doi.org/10.1175/1520-0442\(1992\)005<0561:SVDOWS>2.0.CO;2](https://doi.org/10.1175/1520-0442(1992)005<0561:SVDOWS>2.0.CO;2)
- Webber, B. G. M., Heywood, K. J., Stevens, D. P., Dutrieux, P., Abrahamsen, E. P., Jenkins, A., et al. (2017). Mechanisms driving variability in the ocean forcing of Pine Island Glacier. *Nature Communications*, *8*(1), 14507. <https://doi.org/10.1038/ncomms14507>
- Wingham, D. J., Francis, C. R., Baker, S., Bouzinac, C., Brockley, D., Cullen, R., et al. (2006). CryoSat: A mission to determine the fluctuations in Earth's land and marine ice fields. *Advances in Space Research Series*, *37*(4), 841–871. <https://doi.org/10.1016/j.asr.2005.07.027>
- Zika, J. D., Le Sommer, J., Dufour, C. O., Naveira Garabato, A. C., & Blaker, A. (2013). Acceleration of the Antarctic Circumpolar Current by wind stress along the coast of Antarctica. *Journal of Physical Oceanography*, *43*(12), 2772–2784. <https://doi.org/10.1175/jpo-d-13-091.1>